Nine Martian Years of polar caps observations by SPICAM-IR

A. Lomakin[1,2], A. Fedorova[1], J. R. Berdis[3], O. Korablev[1], J. L. Bertaux[4], F. Lefèvre[4], G. Lacombe[4]and F. Montmessin[4]

[1]Space Research Institute (IKI) RAS, Moscow, Russian Federation
[2]HSE University, Moscow, Russia
[3]Johns Hopkins University Applied Physics Laboratory, Laurel, MD 20723, USA
[4]LATMOS, Sorbonne Université, UVSQ Université Paris-Saclay, CNRS, Paris, France

Key Points:

- We explored the SPICAM-IR dataset consisting of 9 Martian Years of surface observations in order to document the presence of H_2O and CO_2 ices
- The data show a variety of high resolution near-infrared spectra of CO_2 ice from different seasons and latitudes
- The seasonal and spatial maps of CO_2 and H_2O ices allow to track edges of the seasonal caps and to study the influence of global dust storms

Corresponding author: Alexander Lomakin, aleksander.lomakin96@gmail.com

Abstract

SPICAM-IR, an AOTF spectrometer onboard Mars Express spacecraft with a resolving power of 2,000 covering the spectral range 1-1.7 μm has been observing Mars since 2004. In this wavelength range, it is possible to distinguish between CO_2 and H_2O ices and measure their band depths. We obtained about 200,000 high-fidelity spectra of CO_2 ice in different seasons and locations over the Martian polar caps. The spectra have been associated with slab ice, fine-grained ice, permanent caps, and dark and dirty ice at the cryptic region of the south polar cap. Also, we observed more than 200,000 water ice spectra, specifically its broad feature around 1.5 μm. Water ice is present at the surface or in the atmosphere resulting in a variety of different band depths, often in combination with the CO_2 ice. We mapped the equivalent width of 1.43 μm CO_2 ice band and the depth of 1.5 μm water ice band, which are the proxies for grain size, and followed their seasonal evolution. From the maps, we produced the edge (outer crocus line) of the CO_2 south and north caps for nine Martian Years. The cap edges evolve similarly through all years and are in good agreement with previous OMEGA/Mars Express observations. We also discuss the impact of the global dust storms on the cap edges. Lastly, we interpret some of the water ice observations as water ice clouds in the aphelion cloud belt and the polar hoods.

Plain Language Summary

We used data from SPICAM-IR, the instrument on board the Mars Express orbiter, to detect and characterize ices at the surface of Mars. Observing the solar light reflected from the surface in the infrared, SPICAM can capture the presence of carbon dioxide and water ices and differentiate between them. We collected data during 18 years, which translates to 9 Martian Years. This gave us the possibility to study the ices in different seasons and compare results in different years. We tracked the edges of seasonal polar caps to study the effect of two global dust storms, which cover almost all the planet and heat in the atmosphere and the surface. One of these dust storms sped up the recession of the south seasonal cap, the effect already noticed in other observations. The effect of the second one, which was not yet analyzed by other instruments, is not so clear. We have also observed water ice in the atmosphere, the equatorial (so called aphelion cloud belt) and polar clouds.

1 Introduction

Every Martian Year a considerable part of the Martian atmosphere - nearly 25% (Kelly et al., 2006) - condenses into seasonal ice caps that overlay residual caps. That ice consists mostly of CO_2, the main constituent of the Martian atmosphere, with some impurities - water ice and dust. This condensation/sublimation process is one of the major cycles of Mars' climate (Forget et al., 1998; Hourdin et al., 1993). The advance and retreat of seasonal caps have been studied since the first Martian orbiter missions in various spectral ranges. The first infrared instruments determined the constituents of the caps, and VIS cameras monitored their edges (Herr & Pimentel, 1969; Herr et al., 1972). The introduction of thermal infrared (IR) instruments (Christensen et al., 2001; Kieffer et al., 2000) have provided information about climatology of Martian caps over several years. They were also capable of indirectly distinguishing between CO_2 and water ice due to their sharp contrast in surface temperature and could provide some information about grain sizes of ice. The 160-180 K temperature range inferred from these measurements was interpreted both as a sub-footprint variable mixture of CO_2 ice and soil as well as H_2O frost (Kieffer & Titus, 2001). TES also identified the so-called "cryptic region", a dark icy region with CO_2 slab ice covered by a layer of dust (Kieffer et al., 2000).

A new era started with the arrival of the Mars Express in 2003. OMEGA, a hyperspectral imaging spectrometer onboard Mars Express (Bibring et al., 2004) (and CRISM (Murchie et al., 2007) later on MRO), has provided an extensive coverage of polar areas, mapping the expansion and retreat phases of the seasonal caps (Langevin et al., 2007; Appéré et al., 2011; Brown et al., 2010, 2014). Since CO_2 and water ice have diagnostic spectral features in the near-IR and mid-IR, infrared spectrometers can not only effectively identify different types of ices (Bibring et al., 2005), but also could retrieve ice grain size, study mixtures of ices, layers on top of ice and dust contamination (Bernard-Michel et al., 2009). These spectrometers changed the way of observing polar caps, allowing one to map both CO_2 and water ice: for example, the existence of a water ice ring surrounding the receding seasonal south polar cap was confirmed. Spectral reflectance of ices may change dramatically if a photon travels a different path in the material before being reflected. This can then be interpreted in terms of grain size or some combination of granular and slab ice. Retrieving grain sizes requires forward modeling of spectral reflectance and it has been done using multiple models based on different approaches. Most of them are based on radiative transfer (Douté & Schmitt, 1998; Hapke, 1981; Flanner et al., 2007; Andrieu et al., 2018) including a variety of features, such as impurities, layered models and slab models (Andrieu et al., 2018). Others are based on ray tracing and the Monte-Carlo approach (Shkuratov et al., 1999; Bonev et al., 2002). However, in most cases, the models fail to fit observations perfectly. For this reason, many studies (Langevin et al., 2007; Appéré et al., 2011; Brown et al., 2010, 2014) focus on mapping band depth of ices and edges of the seasonal cap and do not attempt to quantify model parameters.

Since spring and summer give the best illumination conditions at the poles, several studies focused on that period and allowed tracking the recession of seasonal polar caps. OMEGA has documented the spatial distribution of band strength of both ices during the recession of both caps and explained the "cryptic region" (Langevin et al., 2007, 2006). The edge of the cap is called the CROCUS line, a concept that was introduced in (Kieffer et al., 2000), and stands as the acronym of "Cap Recession Observations indicate CO_2 has Ultimately Sublimated". The definition was based on thermal IR, and refers to the center of the gap between brightness temperatures of 145K indicative of CO_2 ice and 230K, indicative of bare soil. Since a temperature-based criterion was not applicable to NIR and MIR ranges, (Schmidt et al., 2009) used different approach with OMEGA, defining an outer and an inner crocus lines, corresponding to respectively 1% and 99% of CO_2 ice in a bin. They also summarized previous results and compared with crocus lines derived from TES and OMEGA, and found they were in a good agreement. Another paper, describing seasonal evolution of edges of the caps the in TIR range is (Piqueux et al., 2015). Authors used TES and MCS data to explore multiannual evolution of CO_2 polar ice caps during eight Martian Years, finding little variability between different Martian Years and a general agreement between observations and models. Another topic that has a major impact on Martian climate - global dust storms - is studied. As other instruments (MOC, MARCI, etc.) (Bonev et al., 2002; James et al., 2010), Piqueux et al. (2015) using TES and MCS found that global dust storm can speed up the recession of south seasonal polar cap. This conforms some of the modeling results that predict global (Bonev et al., 2008) increase in sublimation rate, and contradicts others that predict no global or only local effect (Hourdin et al., 1993; Kahre & Haberle, 2010; Bonev et al., 2002). Another instrument that recently documented cap edges and dust storm influence was LNO\NOMAD on Exomars TGO (Cruz Mermy et al., 2022). LNO observed ices in very high resolution ($\lambda/\Delta\lambda$ around 10000) narrow band around 2.335 μm, adding data to the record of IR observations (Oliva et al., 2022). This dataset confirmed OMEGA results, documented MY34 cap edges and impact of GDS, and reported possible detections of CO_2 ice clouds.

One instrument, that has also been capable of observing seasonal trends in the NIR range over several Martian Years is SPICAM-IR (Korablev et al., 2006), AOTF near-

infrared spectrometer on board of Mars Express, covering 9 Martian Years (18 Earth years). With its high spectral resolution, SPICAM resolves CO_2 ice bands in 1-1.7 μm range in detail, showing even very narrow lines that have never been observed by any other spectrometer which has been orbiting Mars up to now. SPICAM-IR nadir data were already successfully used for long-term atmospheric studies, such as water vapor and the O_2 emission mapping (Trokhimovskiy et al., 2015; Guslyakova et al., 2016), but have never been used for analysis of the surface reflectance. IR observations at high spectral resolution may also be useful for detecting impurities in ice, such as PAHs (Campbell et al., 2021).

The present paper is dedicated to retrieving the reflectance of polar ices on Mars and mapping their seasonal distribution. Section 2 describes the instrument, measurements, and the complete dataset. Section 3 describes methods of data processing - correction of gaseous absorption, estimation of ice presence in the field of view, and correction of instrumental effects. Section 4 contains results, spectra of ices from different locations, the seasonal and geographical distribution of ices on Mars, and CO_2 cap edges for both of the poles.

2 Measurements

2.1 Description of instrument

SPICAM is a two-channel spectrometer onboard the Mars Express spacecraft. IR channel is an AOTF (Acousto-Optic Tunable Filter) spectrometer with a resolving power ($\lambda/\Delta\lambda$) varying from 1800 to 2200 and spectral range from 1 to 1.7 μm. Its instantaneous field of view (IFOV) is 1° in nadir, which yields a 5 to 175 km wide footprint covering the surface of Mars. This footprint moves with the motion of MEX, resulting in an elongated FOV, that can be up to 10 times longer than the IFOV. SPICAM-IR has two detectors, working in orthogonal polarizations. For most of the nadir measurements only channel 0 has been used for data analysis due to its higher SNR and its dark current being less sensitive to the detector temperature. SPICAM-IR is an AOTF spectrometer, which means that every spectral point is measured sequentially and at different locations due to FOV motion on the surface. The full spectrum is in 24 seconds. While it is possible to always measure like this, nadir measurements are often performed in several spectral windows to capture objects of interest: O_2 emission (1259 nm - 1287 nm), water vapor (1339 nm - 1440 nm), and ices (1436 nm - 1645 nm). The ice mode is measured for only 6 seconds (996 spectral points), with 5.6 ms for each spectral point, which offers a good compromise between signal-to-noise, length of a footprint on the surface, and sampling rate. Detector noise is higher at the edges of the wavelength range than in the center, which limits the usability of data from 1 to 1.1 μm and from 1.6 μm to 1.7 μm. The sampling rate is higher around 1.38 μm band of water vapor, which was the primary target of observations (Korablev et al., 2006).

Intensity calibration was carried out in flight, using simultaneous observations with OMEGA and is described in Korablev et al. (2006). Up to now there has been no sign of instrument degradation or change in the radiometric response over the years the instrument has operated. The only complexity in the data treatment is a spectral leakage of the AOTF function (which is equivalent to the instrumental function) described in Korablev et al. (2013). However, it has been characterized and is accounted for in the forward modeling of SPICAM NIR observations. Even without correction, it does not significantly affect retrieval of ice spectral albedo due to the strength of the ice bands.

It is important to note that since each SPICAM-IR spectral point is a separate measurement in a narrow spectral filter every point corresponds to a slightly different location on the surface of Mars. If surface albedo changes from one IFOV to the next one, it produces an artificial modulation of the continuum. That may look like a wide absorption line. Other issues affecting the continuum can be variations in the illumination on

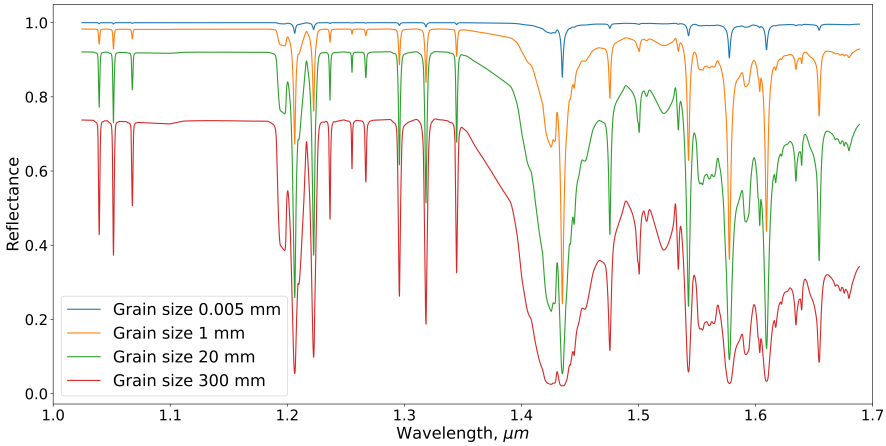

Figure 1. Synthetic spectra of CO_2 ice with different grain sizes simulated with the Hapke model. The model is the same as in Berdis et al. (2022). Note that the 300 mm grain size is likely close to slab ice.

the surface or shadows from the terrain, producing an apparent change in albedo. This problem is specific to AOTF spectrometers since diffraction grating-based spectrometers acquire all points of the spectrum simultaneously.

2.2 Dataset

SPICAM-IR started to work in nadir and spot-tracking mode at the end of Martian Year 26 (January 2004) and covers all years until Martian Year 35 producing around 600 orbits per Martian Year, totaling more than 5500. Because the instrument has no spatial resolution, it is difficult to resolve the geographical structure of polar caps. Still, it is possible average several MY to gather more data or just study specific Martian Years with good coverage of needed season. Mars Express orbit is almost polar, with the pericenter at 298 km and the apocenter at 10107 km. The same region is revisited every 11 orbits, with a slight longitudinal shift in between. The dataset covers two global dust storms - in years 28 and 34 and the full recession of both caps in several years. Years 30-34 were covered more sparsely and years 32-34 exhibit only patches of south cap recession. On the other hand, MY33 is the only year when the edge of condensation of the south polar cap was observed. Also, the cryptic region and its evolution were observed in different seasons and different Martian Years.

3 Methods

3.1 Detecting ice

Both CO_2 and water ice are easily detectable in the NIR range. CO_2 ice has a set of sharp features, most notable around 1.4 μm and 1.6 μm (Hansen, 2005; Quirico & Schmitt, 1997) as can be seen on Fig. 1. H_2O ice has a broad absorption band centered around 1.5 μm (Grundy & Schmitt, 1998). Both ice spectra exhibit a huge variability depending on impurities (dust, intermixing with ices) and photon path length (which is proportional to grain size). The grain size effect is shown in Fig. 1 for CO_2 ice. It should be noted that in some cases the 1.6 μm carbon dioxide band can be confused with water

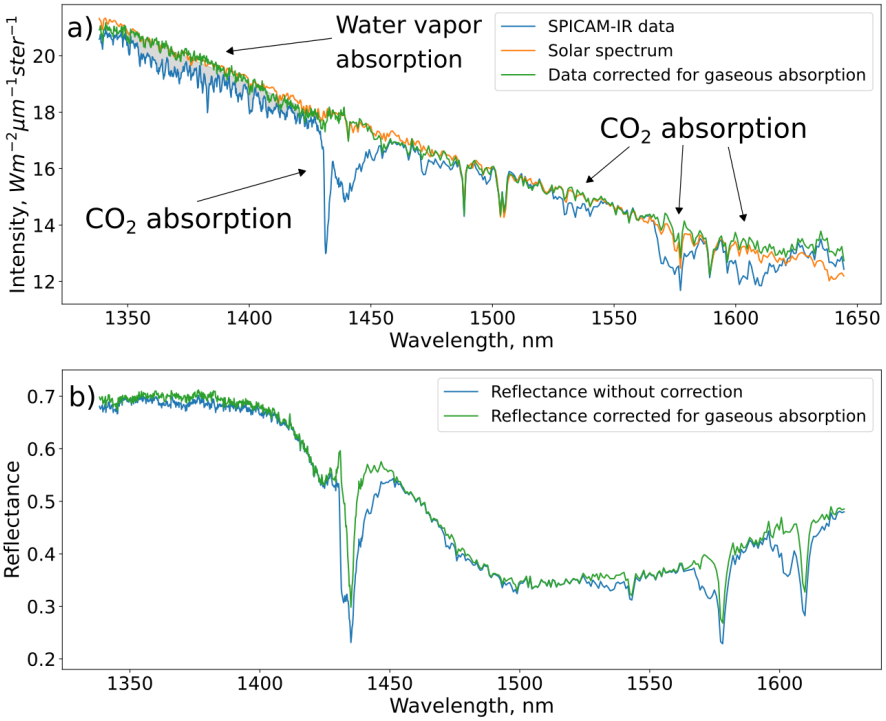

Figure 2. (a) Comparison between intensity measured by SPICAM-IR (blue line) spectrum, CAVIAR solar spectrum (orange line), and SPICAM-IR data corrected for gaseous absorption (green line). Water vapour absorption is shaded. All spectra are offset to match SPICAM-IR data for the sake of clarity. (b) Comparison between reflectance obtained without gaseous correction (blue line) and with correction (green line). It is shown that the absence of correction will impact the retrieval of band strength hugely.

ice reflectance. Both ices can be detected in raw data, atmospheric corrected data lowers the detection threshold.

3.2 Correction of atmospheric absorption

Since 1.4 μm CO_2 ice band is intersecting the 1.43 μm gaseous absorption of atmospheric CO_2, it is necessary to model the transmission of atmosphere. Its contribution is calculated using Beer-Lambert law:

$$I = I_0 exp(-\tau(\lambda)) \tag{1}$$

I is measured spectrum, I_0 is solar radiation, optical thickness τ:

$$\tau(\lambda) = \int_0^\infty \sigma(\lambda, z) n(z) (\frac{1}{\mu} + \frac{1}{\mu_0}) dz \tag{2}$$

μ and μ_0 are cosines of incidence and emission angles,

σ is the absorption cross-section of the gas and n is the concentration of gas on the optical path. We calculate cross-sections using HITRAN-2016 (Gordon et al., 2017) with Voigt approximation (Humlíček, 1982). The atmosphere is divided into 50 layers, and the parameters of each layer are retrieved from MCD 5.3 (Millour et al., 2015). We take into account both CO_2 and water, the only gases that have absorption on our wavelength

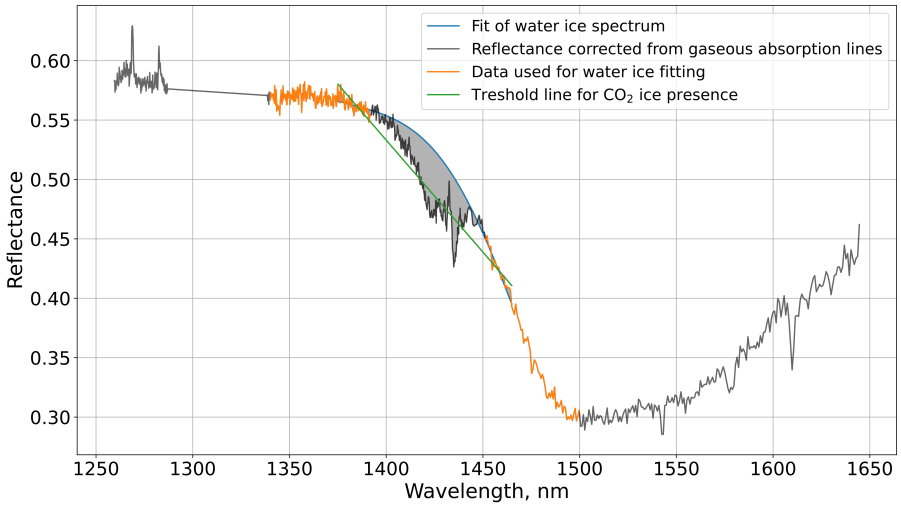

Figure 3. Example of correction from water ice continuum. The shaded area represents integral for calculating equivalent width. On this spectrum, a few steps of the correction algorithm from section 3.2 were applied.

range. Most notable absorption bands are 1.43, 1.58 and 1.6 μm for CO_2 and 1.38 μm for water vapor - all of them can be seen in the figure 2. We use a water vapor mixing ratio vertical profile from MCD 5.3. Spectral reflectance is then calculated:

$$R = \frac{I(\lambda)}{\frac{I_{solar}}{(SM_{dist})^2}\frac{\mu_0}{\pi}e^{-\tau(\lambda)}} \tag{3}$$

where ϕ_λ is solar spectrum at 1 a.u., SM_{dist} is Solar-Mars distance in a.u., μ_0 is the cosine of solar zenith angle. In the case of SPICAM-IR with the high spectral resolution, it is important to have precisely measured solar spectrum, since any discrepancies in solar spectrum and data affect the quality of reflectance. We use CAVIAR solar spectrum (Menang et al., 2013), which is measured through the Earth's atmosphere. The result of the atmospheric correction can be seen on Fig. 2.

3.3 Estimate of the ice band strength

Indexes of the band depth are widely used in studying ices on Mars. OMEGA and CRISM used a depth of 1.43 μm CO_2 ice band since it is much less saturated than others (Langevin et al., 2007; Appéré et al., 2011; Brown et al., 2014). This index reflects not only the presence of CO_2 ice, but also parameters such as grain size, dust/water inclusions, and ice percentage in FOV. In the case of OMEGA spectral resolution, the band is described by a few spectral points. SPICAM has a much better sampled band, which requires the choice of different metrics. While the minimal value of 1.43 μm band can be used for slightly more sensitive detection, it gets saturated easily, preventing to retrieve ice parameters and therefore ice evolution on the surface. We use an equivalent width as a more flexible way to measure band strength:

$$Q_{CO_2} = \int (1 - R(\lambda)/R_{continuum})d\lambda \tag{4}$$

$R_{continuum}$ is the reflectance of continuum averaged from 1.367 to 1.375 μm. The equivalent width shows the strength of the spectral feature and is measured in units of wave-

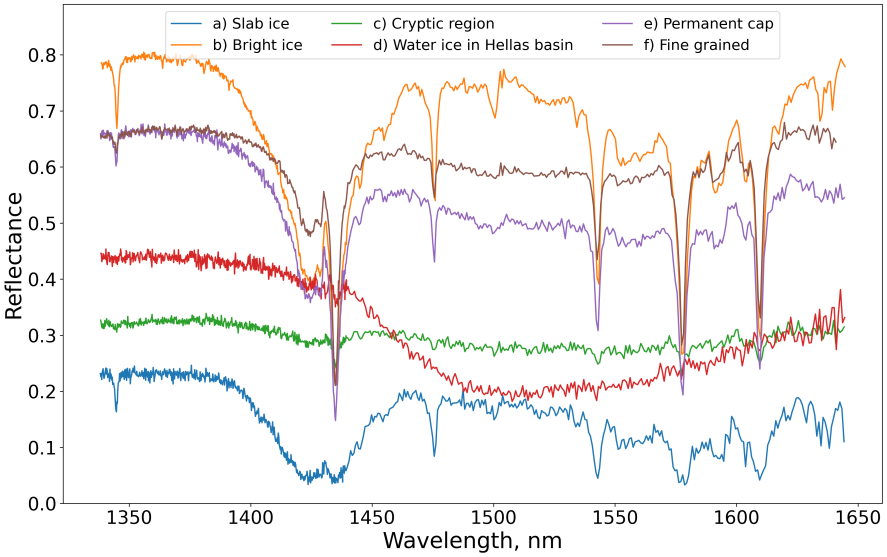

Figure 4. Diversity of ice spectra on south pole. **a) Blue**: Slab ice in winter, L_s: 144.15, latitude: -58.7, longitude: 257.58, orbit: 10902A01, 1.43 μm band width: 30.5 nm; **b) Orange**: Bright CO_2 ice, L_s: 253.08, latitude: -86.23, longitude: 315.70, orbit: 1943A01, 1.43 μm band width: 16.4 nm; **c) Green**: Cryptic region with almost no CO_2 ice, L_s: 213.12, latitude: -82.52, longitude: 122.06, orbit: 4169A01, 1.43 μm band width: 1.4 nm; **d) Red**: Water ice outside of cap in winter in the Hellas basin, L_s: 117.01, latitude: -42.97, longitude: 83.266, orbit: 20144A03, water ice index: 0.47; **e) Purple**: South permanent cap in the middle of summer, L_s: 322.85, latitude: -86.06, longitude: 311.33, orbit: 19015A01, 1.43 μm band width: 12.1 nm; **f) Brown**: Fine grained CO_2 ice in the spring, L_s: 195.30, latitude: -64.90, longitude: 298.47, orbit: 8867A01, 1.43 μm band width: 6.6 nm

length, in our case - in nanometers. Due to SPICAM-IR observations being very dense in observing spectral signatures, there are a few spectral regions that can be used for robust automatic continuum evaluation. We chose the 1.37 μm range because it lies outside of CO_2 ice absorption bands, broad water ice absorption band, 1.27 μm O_2 singlet delta airglow ($^1\Delta g$) and does not overlap with major solar lines, not to have any effect in possible wavelength misalignment. Metrics for water ice are more straightforward due the flatness of the band:

$$Q_{H_2O} = 1 - \frac{R_{1465} + R_{1490} + R_{1510}}{3R_{continuum}} \tag{5}$$

Where R_λ is reflectance at λ (nm). Three regions are chosen to limit the influence of noise and are picked around minor CO_2 ice bands. It should be noted, that CO_2 ice with long photon path lengths may result in a small amount (up to 0.12) in this index due to some absorption values in this region (see Fig. 1 and section 3.1).

A more annoying problem arises when evaluating the band depth of CO_2 ice, which is superimposed to a wide water ice band. In that case, a multiple-step algorithm is performed. In any spectrum containing water ice absorption, the presence of CO_2 ice 1.43 μm band is checked first. If it is present - the width of the band is calculated iteratively, adjusting the continuum shaped by water ice at every iteration. Then the width of the

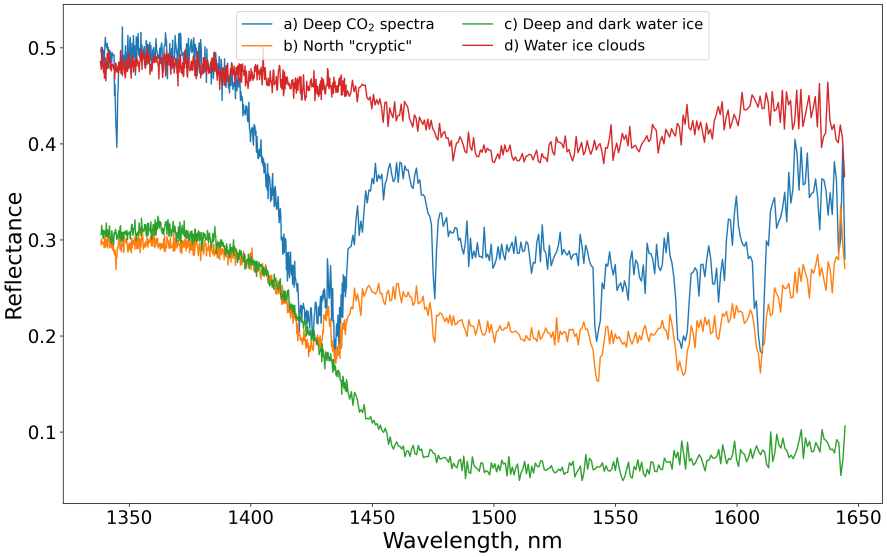

Figure 5. Diversity of ice spectra on north pole and spectrum of water ice clouds. **a) Blue**: Deep CO_2 ice on North pole, L_s: 14.48, latitude: 85.72, longitude: 134.13, orbit: 5161A01, 1.43 μm band width: 20.6 nm; **b) Orange**: "Cryptic"-like spectra in the end of winter, L_s: 332.38, latitude: 57.47, longitude: 82.96, orbit: 19074A01, 1.43 μm band width: 10.45 nm; **c) Green**: Spectrum with high water ice index on North pole, L_s: 107.88, latitude: 84.74, longitude: 34.69, orbit: 1002A01, water ice index: 0.758; **d) Red**: Water ice cloud in aphelion cloud belt, L_s: 114.94, latitude: 11.98, longitude: 254.08, orbit: 8336A01, water ice index: 0.146;

band can be calculated (see Fig. 3). A detailed description of the algorithm can be found in appendix.

Yet another problem appears because of the AOTF spectral points acquisition, as described in the section 2.1. This may produce features that the algorithm may identify as water ice or even CO_2 ice. To overcome these false positives we use an algorithm that helps decrease their number. We mark the spectrum as distorted by the AOTF if:

1. There is a slope in reflectance between 1.30 and 1.37 μm
2. There is a slope in reflectance between 1.36 and 1.37 μm
3. If reflectance at any of the 1.465, 1.49, and 1.51 μm is more than $1.2R_{continuum}$

Since these regions do not cover the whole spectral range, the spectrum may be distorted in other areas, though we greatly reduce number of false positive detections. We can decrease this ratio to even smaller amounts by rejecting observations with low spacecraft altitude, and thus a small FOV footprint on the surface (by reducing the impact of surface roughness on the spectra acquisition). This procedure makes the impact of these problems relatively marginal.

Index of water ice makes no distinction between water ice on the surface and in the atmosphere. However, the 1.5 μm band is not very sensitive to water ice clouds, and SPICAM-IR can be used for water ice cloud detection in a very limited way. Nevertheless, in some areas - like the aphelion cloud belt - we can clearly observe water ice clouds. The detec-

tion limit of water ice in atmosphere varies (Q_{H_2O} ~0.08-0.12) from season and latitude and is connected with the atmospheric dust spectral slope. Though, water ice clouds cannot have more than a certain optical thickness. While the exact determination of these values and generally a distinction between water ice clouds and water ice on the surface are out of the scope of this paper, we would consider a value of $Q_{H_2O} \sim 0.12$ as a rough detection threshold for surface water ice presence, based on maximum bands depth reported by OMEGA (Langevin et al., 2007).

4 Results

4.1 Diversity of ice spectra observed with SPICAM-IR

Since CO_2 ice on Mars was never measured with resolving power ~ 2000 in this spectral region, we present a few signatures from different regions of polar caps at various seasons. CO_2 ice reflectance varies a lot with grain size (as shown in Fig. 1), ice impurity, and dust percent.

South pole: Key spectral classes on Mars south pole were identified by OMEGA (Langevin et al., 2007). First is a very low albedo spectrum with very strong CO_2 signatures (~30-38 nm equivalent width of the 1.43 μm band: shown on Fig. 4, a). Langevin et al. (2007) identified them as clean CO_2 slabs overlaying surface on seasonal cap. We observe these features in winter all over the cap, as close to the center of it as coverage allows (see detections on Fig. 6). Another spectral class with a less strong equivalent width of the 1.43 band of CO_2 ice (20-25 nm), but with higher albedo (up to 0.75) is observed mostly during the seasonal cap recession in spring (Fig. 4, b). There are also many spectra with equivalent width of the 1.43 μm band ranging from 6 nm to 38 nm. Patches with relatively high albedo (0.6-0.7) and narrow band CO_2 ice are observed during early spring near the edge of the south cap, which probably corresponds to relatively clear and fine grained CO_2 snow (Singh & Flanner, 2016; Langevin et al., 2007) (Fig. 4, f). Another object of interest is the "cryptic region", where there are almost no signatures of CO_2 ice deep into the south seasonal cap during early spring (Fig. 4, c). This region is described and discussed in several papers (Kieffer et al., 2000; Langevin et al., 2006). Kieffer et al. (2006) suggested an eruptive venting process that propels and disseminates soil particles over the transparent CO_2 slab thereby masking CO_2 ice signature. We observe this region in Martian Years 28-35 except for year 34 because of the absence of coverage of that area. Signatures with the lowest amount of CO_2 ice signatures are observed mostly in Martian Year 28, probably because Martian Year 28 exhibits the best coverage of the cryptic region.

There are also water ice signatures on the South pole. For some observations, we can attribute them to ground ice, though the accurate distinction between water ice or snow on the surface of Mars and clouds cannot be made so distinctly. Medium deep (0.3-0.35) water ice signatures at the South pole are observed during the recession from $L_s = 160°$ to $L_s = 230°$. There are also a few observations of H_2O ice signatures with no or small amount of CO_2 ice in the "cryptic region" in MY 28 and in Hellas basin in different MY (Fig. 4, d). The water ice index in these observations also varies between 0.3 and 0.35. The highest index (0.5-0.55) on the south pole was observed during winter at the edge of the seasonal cap or even out of it on the Hellas basin in combination with CO_2 ice signatures. As discussed by Langevin et al. (2007); Appéré et al. (2011); Singh and Flanner (2016) all of these signatures on the cap may be interpreted as either contamination of CO_2 ice with water ice grains or a thin layer of water ice frost on top of carbon dioxide.

The last object of interest on the South cap is the permanent cap, which was observed in Martian Years 27, 28, 29, 33, 34, 35. Most of the observations present strong, quite bright CO_2 ice signatures with occasional water ice inclusions (Fig. 4, e).

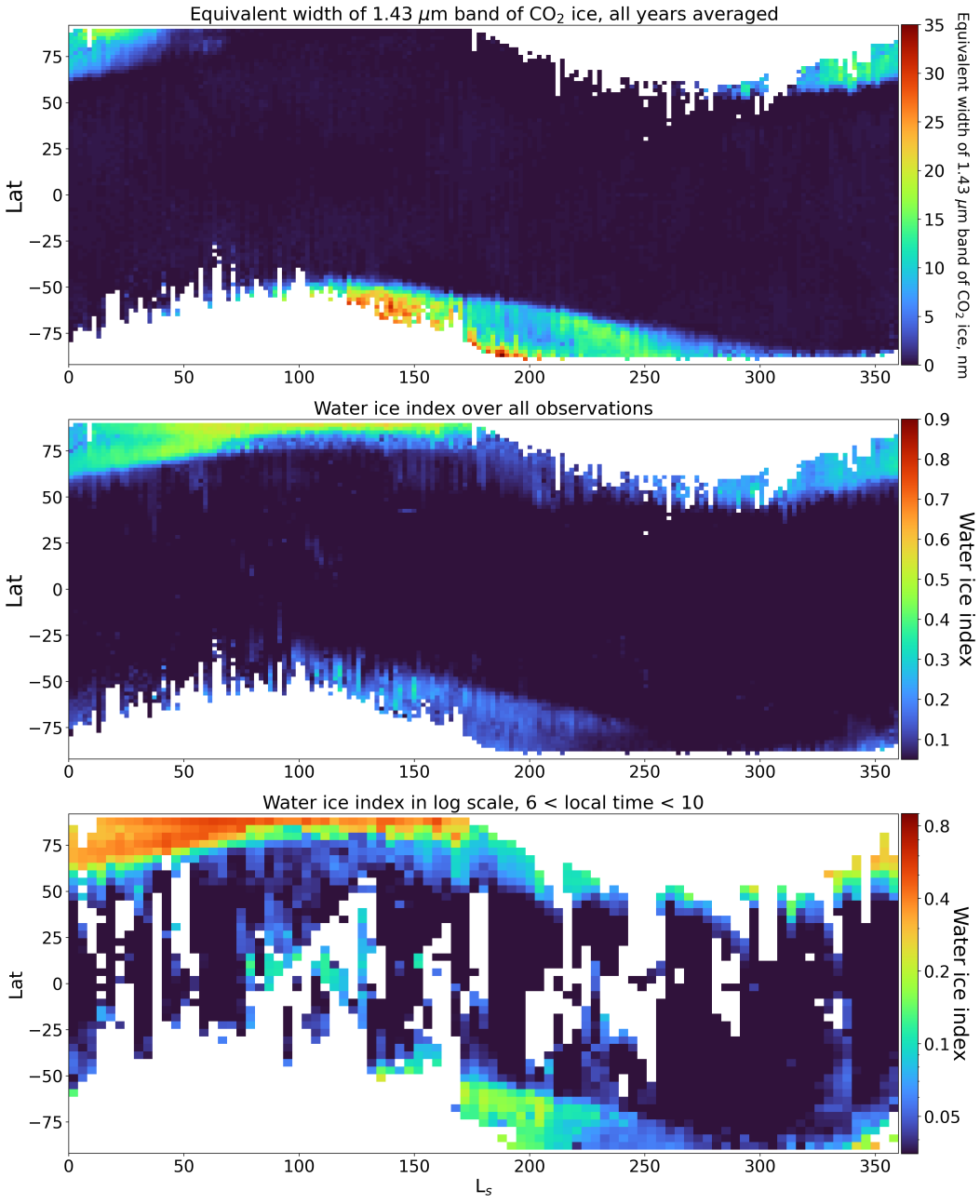

Figure 6. Seasonal maps of CO_2 1.43 μm equivalent width (top), water ice index (middle), and water ice index in log scale for the morning (bottom).

North pole: The north pole does not present such a variety of spectral signatures. Still, there are also "cryptic"-like spectra around $L_s = 330°$ - $L_s = 355°$ with low albedo (0.3-0.4) (Fig. 5, b) and strong CO_2 ice signatures mixed with strong water ice signatures (Fig. 5, a). It significantly brightens in spring with a maximum equivalent width of 1.43 μm band of 20 nm from $L_s = 10°$ to $L_s = 20°$. Otherwise, there is little variety in CO_2 signatures, with the maximum equivalent width being around 21 nm.

This result is expected because the north pole is more "wet" than the south pole. However, the water ice spectrum does not present much diversity, but there are some interesting spectra of H_2O ice: for example, low albedo, but deep water ice signatures (Fig. 5, c) on perennial north pole ($L_s = 100°$-$130°$). Water ice index may be as high as 0.8 at around $L_s = 110°$.

All of these spectra have the potential for accurate and high precision retrievals of parameters: the grain size, identifying slab ice, dust content, and water ice impurity. Complicated layered models may be considered to fit observed spectra precisely. This in-depth exploration lies out of the scope of this paper, yet will be the topic of future work with SPICAM-IR data.

Lastly, we also observe water ice clouds in our spectra (Fig. 5, d). Water ice features are clearly observed near the aphelion cloud belt and on both poles outside the polar cap. The geographical distribution of these detections also matches patterns reported by Szantai et al. (2021). However, However, the sensitivity of detection in the 1.5 μm band is significantly lower than 3.1 μm.

4.2 Seasonal map and average ice distribution

One way to characterize seasonal polar caps with SPICAM-IR observations is to average observations for all longitudes and plot a seasonal map of the equivalent width of CO_2 ice and water ice band depth in L_s - latitude axis (Fig. 6). This shows the seasonal dynamics and leverages on the complete SPICAM-IR dataset. These maps also illustrate the coverage for every Martian Year (see Supporting Information). Map of the equivalent width of 1.43 μm band of CO_2 ice (Fig. 6, top panel) shows the seasonal evolution of CO_2 ice by combining all years. Coverage of the recession of the south seasonal polar cap is good, the only year with bad coverage of it is MY33 (see Figures S2-S7 from Supporting Information). Still, after $L_s = 220°$ the recession is asymmetric and the edge of the cap is not well defined. The recession of the north seasonal cap is also well documented and was observed in years 29, 30, and 35. Coverage of the expansion phase of both seasonal polar caps is much more patchy due to the observation conditions. As for the south seasonal cap, pieces are seen in different years, though most of the observations belong to year 33. North pole expansion phase coverage is also patchy for the same reasons.

Water ice seasonal maps (Fig. 6, middle panel) can provide a little less information, due to lower sensitivity to water ice than CO_2 ice. Nevertheless, we can monitor the edge of the north polar cap and be able to detect the presence of clouds. The averaged distribution of water ice index shows recession of north polar cap and also strong detections on the south pole. While some of the weak detections during the recession of the south polar cap can clearly be attributed to water ice frost on the surface, some others may be confused with clouds or very strong CO_2 ice. Another thing that is clearly seen on this map divided by local time (Fig. 6, bottom panel) is the aphelion cloud belt. This distribution also closely matches clouds detected by OMEGA (Szantai et al., 2021; Olsen et al., 2021).

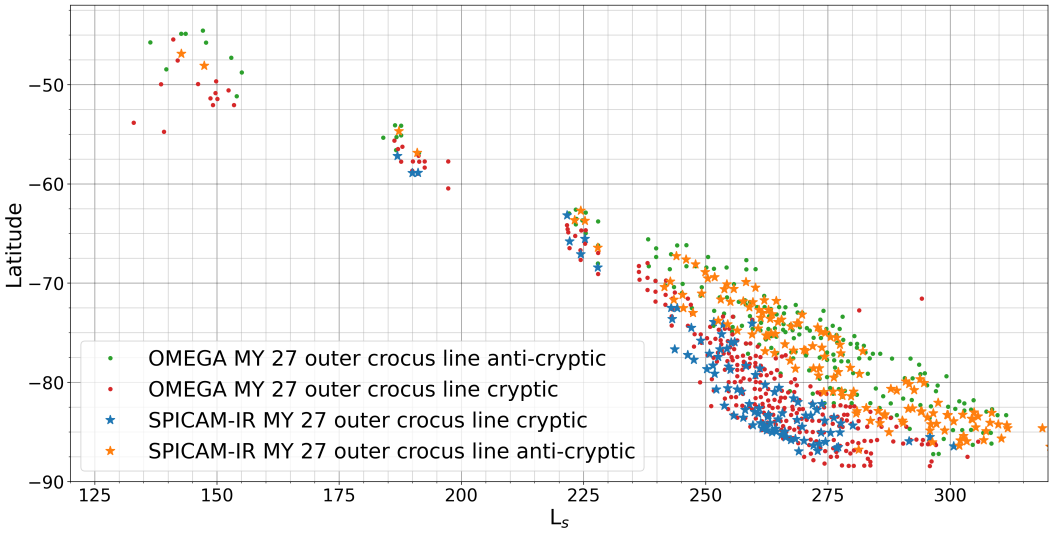

Figure 7. The outer crocus line by SPICAM-IR and OMEGA are both cryptic and anti-cryptic parts of the polar cap for Martian Year 27. Data on OMEGA outer crocus line taken from Schmidt et al. (2009)

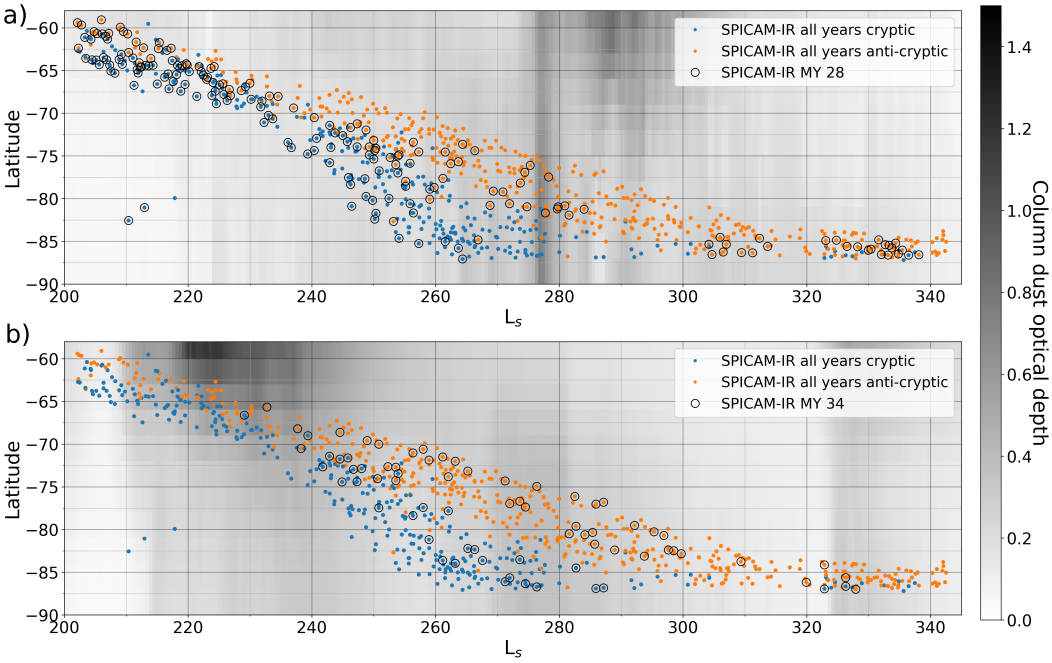

Figure 8. Outer crocus line by SPICAM-IR both cryptic and anti-cryptic parts. Circled points are from Martian Year 28 in figure a and from Martian Year 34 in figure b. On the background plotted the daily column-integrated dust scenarios for corresponding Martian Year (Montabone et al., 2015, 2020)

4.3 Edge of the cap

Another result that can be retrieved from the SPICAM-IR data is the edge of the cap, or rather, the crocus line. This subject is widely discussed by Schmidt et al. (2009): using OMEGA data it was shown that the crocus line is different for cryptic (from 60° to 260° east longitude) and anti-cryptic parts (from 260° to 60° east longitude) of the south polar cap. OMEGA coverage allows distinguishing between them. Authors of the paper also differentiate between inner and outer crocus lines: inner means bin with lower than 99% of pixels with CO_2 ice coverage which is closest to pole and outer means pixel with at least 1% of pixels that are covered with CO_2 ice that is closest to the equator. With SPICAM-IR, we cannot determine the "CROCUS line", which is specific to thermal IR instruments, neither the "inner crocus line", because it is very hard to distinguish between subpixel mixing of CO_2 ice and soil and small grain size. But we can determine the outer crocus line, which corresponds in our case to the first detection of CO_2 ice on our track (for more details see appendix). For consistency and comparison with previous measurements by OMEGA (Fig. 7) we use the same definitions as in previous works. The detections are very consistent for both instruments and show close correlation.

As for seasonal variations, both north and south CO_2 cap behavior is very consistent from year to year, similar to Piqueux et al. (2015) and Schmidt et al. (2009). Though, it is known that global dust storms have an effect on the south polar cap recession (Bonev et al., 2002; Bonev et al., 2008; Piqueux et al., 2015). SPICAM-IR captured two dust storms (Fig. 8) that took place in different seasons: MY28 in southern summer (L_2 270°-320°) and MY34 in spring southern (L_2 200°-270°). The impact of the MY28 dust storm was already documented by MCS (Piqueux et al., 2015) and MARCI (James et al., 2010; Calvin et al., 2017). Both instruments observed smaller cap extent compared to non-dusty years, but since it was already the end of the recession, the mass of sublimed CO_2 was not too big (authors aim to measure mass of CO_2 rather than cap edge). However, these late dust storms are something that may impact the layer of CO_2 on the residual cap and also affect its stability. The effect of the MY28 on cap edge measured by the SPICAM-IR can be seen in Fig. 9, showing less extent compared to the climatology. The MY34 dust storm was not reported by any instrument but is very close to the MY25 GDS in atmospheric dust loading and timing (Montabone et al., 2020). TES in MY25 (Piqueux et al., 2015) reported global acceleration of the recession of the polar cap in bright areas (anti-cryptic part of the cap) starting from the $L_s = 190°$ to $L_s = 225°$. In MY34, SPICAM-IR performed first observations of the seasonal cap edge around $L_s = 230°$, showing no effect or even a little more extent of seasonal cap compared to climatology (Fig. 8). This discrepancy can be explained by two reasons: the timing of SPICAM-IR observations is after the end of the accelerated recession observed by TES and different definitions of cap edge. Piqueux et al. (2015) reported less extent of CROCUS line, but the CO_2 frost cover was the same (or even greater) as in non-dusty years. Since we define the cap edge as the last detection of CO_2 ice, it may not reflect the accelerated recession in the same way as TIR instruments do.

North polar cap was also reported to be impacted by a dust storm (Piqueux et al., 2015). It is much harder to observe effect of them on north pole because the dusty season occurs during the fall and winter in the northern hemisphere and thus the polar night at high latitudes. Otherwise, there are not many variations between different years (see Fig. 10).

4.4 Mapping ices distribution

While SPICAM-IR was not designed as a mapping spectrometer and measures only along-track, we still can construct spatial maps (figure 11, Figure S1 in Supporting Information). One of the features that is clearly seen with this data representation is the cryptic region in the southern hemisphere. Only two years have enough coverage of the

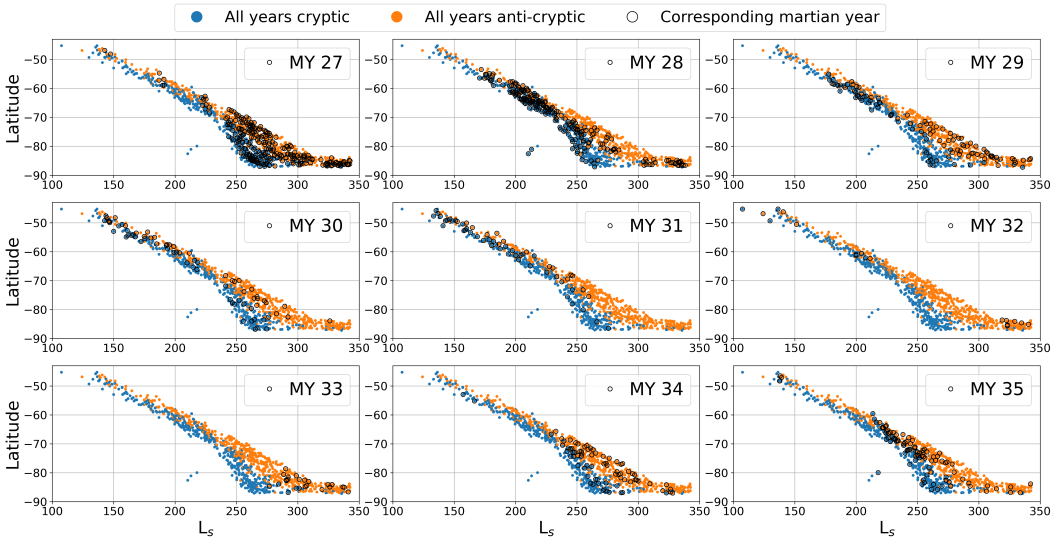

Figure 9. Outer crocus line for the south cap for all Martian Years combined. Orange points represent anti-cryptic part (from 260° to 60° east longitude) and cryptic part (from 60° to 260° east longitude). Data from these pictures is available in the Supporting Information.

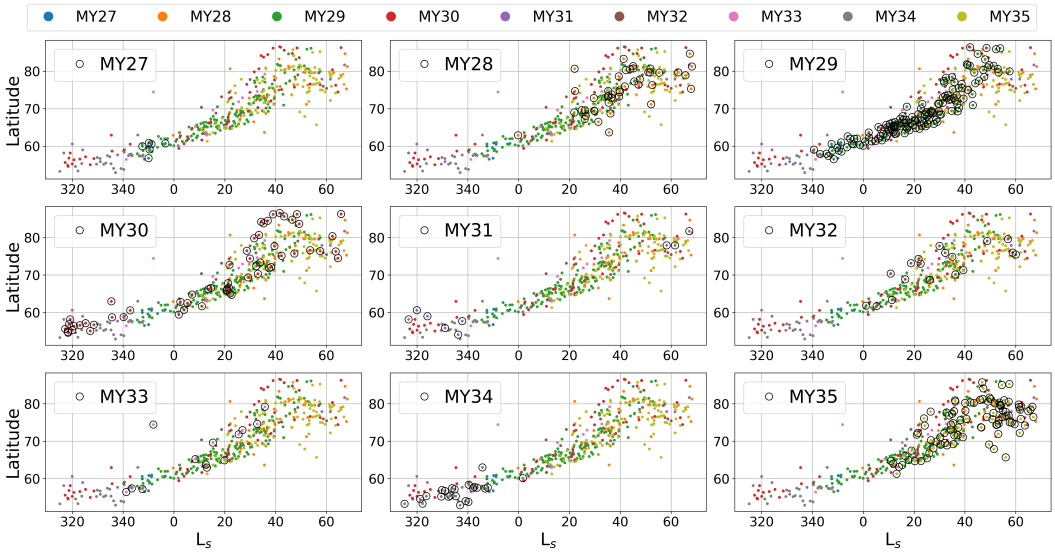

Figure 10. Outer crocus line for the north cap for all Martian Years combined. Different colors represent different Martian Years. Data from these pictures is available in the Supporting Information.

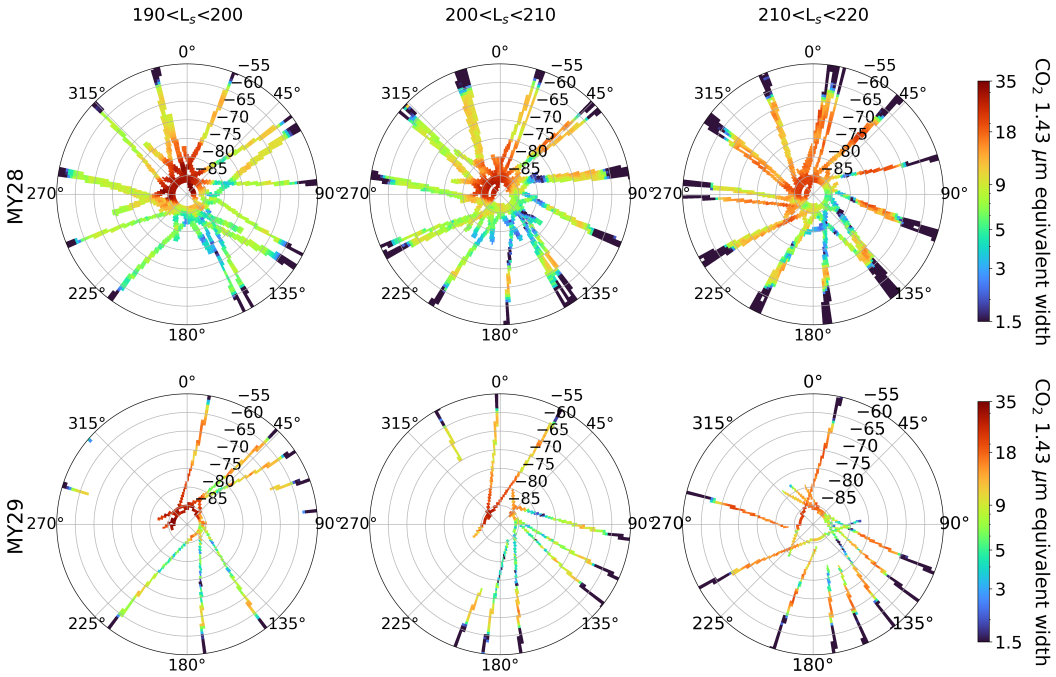

Figure 11. Map of CO_2 1.43 μm equivalent width in logarithmic scale for Martian Years 28 and 29 binned by 1.4 by 0.7 degrees in south polar projection.

cryptic region, these are 28 and 29. While other years contribute to monitoring cap edge and seasonal maps, their spatial coverage does not allow to observe any structures. Our limit of detection (see appendix) is 1.5 nm and it can clearly be seen that between L_s = 200° and L_s = 210° there are regions that are close to the detection limit of SPICAM-IR. While the cryptic region in year 28 resembles what was seen by OMEGA in Martian Year 27 (Langevin et al., 2007), data from Martian Year 29 shows a moderate correlation with both previous year and OMEGA observations.

5 Conclusion

We used the calibrated 1B level SPICAM-IR spectra to produce reflectance data throughout all nine Martian Years of observations. To obtain the reflectance, we corrected for the atmospheric gaseous absorption using Mars Climate Database 5.3 and HITRAN2016.

We obtained about 200,000 high-resolution ($\lambda/\delta\lambda \sim 2{,}000$) high signal-to-noise spectra of CO_2 ice in different seasons and geographic areas of Martian polar caps. These spectra include slab ice, fine-grained ice, spectra of permanent caps, and spectra of dark and dirty ice at the cryptic region of the south polar cap of Mars. Also, we were able to observe water ice spectra, specifically the 1.5 μm wide band. We observed it on the surface and in the atmosphere and obtained a variety of different spectra of water ice, usually combined with CO_2 ice.

We were also able to quantify ice presence with different metrics, the equivalent width for the CO_2 ice and the band depth index for the water ice. We have used slightly modified index of H_2O ice as used for OMEGA and CRISM analysis (Langevin et al., 2007; Appéré et al., 2011; Brown et al., 2014). We composed seasonal maps of these quantities and obtained an average seasonal distribution allowing to track the spring recession of both caps in detail. SPICAM-IR appears to be sensitive to water ice clouds in

nadir, though we are not always able to distinguish the atmospheric signature from ground ice or impurities in CO_2 ice. We were also able to obtain spatial maps of ice distribution on the surface for two Martian Years, showing the formation and evolution of the cryptic region, though sparsely. Lastly, we produced the edge (outer crocus line) of CO_2 south and north cap. SPICAM-IR observations showed very consistent cap edges and the impact of two global dust storms. MY 28 dust storm did speed up the end of the recession of the south polar cap, which is consistent with thermal data and modeling, though the effect of MY 34 global dust storm was not so clear, possibly because of the limited coverage. We compared our data with OMEGA observations in MY 27 (Schmidt et al., 2009), revealing a good agreement between the two instruments.

There is still an unexplored potential in SPICAM-IR data. Next steps with this dataset may be retrieving ice parameters using models of spectral reflectance and analyzing co-located observations with other instruments (SPICAM-UV, OMEGA, and CRISM). There is also an opportunity to analyze more precisely water ice cloud distribution. The whole dataset already contains around 1.5 million spectra of the martian surface and continues to grow.

Data Availability Statement

SPICAM 1A and 1B data used is available at ESA Planetary Science Archive (PSA): https://archives.esac.esa.int/psa/#!Table%20View/SPICAM=instrument. Indexes for CO_2 and H_2O ices (and other metadata) for each orbit with signal-to-noise ratio more than 20 is available at https://doi.org/10.5281/zenodo.7082888. Data from Figures 4-6, 9 and 10 is also available at https://doi.org/10.5281/zenodo.7082888. Data from Figure 7 is can be found in Schmidt et al. (2009), dust optical depth from Figure 8 can be found at http://www-mars.lmd.jussieu.fr/mars/dust_climatology/index.html.

Software Availability Statement

MCD5.3 used for atmospheric correction is available at http://www-mars.lmd.jussieu.fr/mars/access.html

Appendix A Estimating carbon dioxide ice band depth when water ice is present

In the case of both ice signatures present in the spectrum (4, e or 5, a), it is important to accurately subtract the water ice spectrum. This is done in a few steps:

1. Identify if water ice is present in the spectrum; if not present - proceed to the straight evaluation of the band with equation 5
2. Normalize spectrum by dividing the whole spectrum on $R_{continuum}$
3. Select two regions which are out of the main CO_2 ice absorption band. As the first step, the first region is 1.367 - 1.375 μm and the second is 1.465 - 1.475 μm
4. Calculate linear interpolation between mean reflectance of these regions
   (a) If 40% of points in reflectance spectrum between these two regions are located below this interpolation line - CO_2 ice is present
   (b) If not - offset both spectral regions by 2 nanometers closer, repeat from the start of point 4
   (c) If this shift is 20 nm - there is no CO_2 ice
5. Find signal to noise ratio of the spectrum to find the degree of polynomial to fit the spectrum
   (a) If signal to noise is less than 20 - degree=1
   (b) If signal to noise is less than 45 - degree=2

(c) Else - degree=5

6. Fit the region (from 1.34 to 1.375+offset·1.2 μm and from 1.465-offset to 1500 μm) with a polynomial of a chosen degree. In the majority of cases degree is 5.
7. Evaluate polynomial with retrieved parameters at CO_2 band region, subtract if from spectrum and proceed to equation 5

This procedure proved to be very robust and produced stable results in almost every case. The sample result can be seen in figure 3 and Movie S2 in Supporting Information.

Appendix B Cap edge detection method

For every orbit which has at least 5 detections of CO_2 ice, we take the track and split it in half by the point of minimum (or maximum) latitude. Then we use sliding windows with a size of 5 and look at how much of the observations in this window meet the threshold of CO_2 ice detection ($\sim$2 nm equivalent width of the band). If 3 out 5 of the observations in this window meet the threshold, then all of the points in the window are marked with CO_2 ice presence. The outer crocus line is the point closest to the equator for each track. Sometimes, orbit ends (or starts) in the middle of the cap - in that case, we check if the outer crocus line is the last or first point in the orbit - if it is true, that point is rejected. If this point longitude is from 60° to 260° east longitude, then we say it belongs to the cryptic part of the pole, otherwise, it belongs to the anti-cryptic part.

References

Andrieu, F., Schmidt, F., Douté, S., & Chassefière, E. (2018). Ice state evolution during spring in richardson crater, mars. *Icarus*, *315*, 158 - 173. Retrieved from `http://www.sciencedirect.com/science/article/pii/S0019103517305274` doi: https://doi.org/10.1016/j.icarus.2018.06.019

Appéré, T., Schmitt, B., Langevin, Y., Douté, S., Pommerol, A., Forget, F., ... Bibring, J.-P. (2011). Winter and spring evolution of northern seasonal deposits on mars from omega on mars express. *Journal of Geophysical Research: Planets*, *116*(E5). Retrieved from `https://agupubs.onlinelibrary.wiley.com/doi/abs/10.1029/2010JE003762` doi: 10.1029/2010JE003762

Berdis, J. R., Murphy, J. R., & Chanover, N. J. (2022, February). Europa's Surface Water-ice Crystallinity and Correlations between Lineae and Hydrate Composition. *The Planetary Science Journal*, *3*(2), 36. doi: 10.3847/PSJ/ac4cb6

Bernard-Michel, C., Douté, S., Fauvel, M., Gardes, L., & Girard, S. (2009). Retrieval of mars surface physical properties from omega hyperspectral images using regularized sliced inverse regression. *Journal of Geophysical Research: Planets*, *114*(E6). Retrieved from `https://agupubs.onlinelibrary.wiley.com/doi/abs/10.1029/2008JE003171` doi: 10.1029/2008JE003171

Bibring, J.-P., Langevin, Y., Gendrin, A., Gondet, B., Poulet, F., Berthé, M., ... the OMEGA team (2005). Mars surface diversity as revealed by the omega/mars express observations. *Science*, *307*(5715), 1576–1581. Retrieved from `https://science.sciencemag.org/content/307/5715/1576` doi: 10.1126/science.1108806

Bibring, J.-P., Soufflot, A., Berthé, M., Langevin, Y., Gondet, B., Drossart, P., ... Forget, F. (2004, 07). Omega: Observatoire pour la minéralogie, l'eau, les glaces et l'activité. *European Space Agency, (Special Publication) ESA SP*, *1240*, 37-49.

Bonev, B. P., Hansen, G. B., Glenar, D. A., James, P. B., & Bjorkman, J. E. (2008, February). Albedo models for the residual south polar cap on Mars: Implications for the stability of the cap under near-perihelion global dust

storm conditions. *Planetary and Space Science*, *56*(2), 181-193. doi: 10.1016/j.pss.2007.08.003

Bonev, B. P., James, P. B., Bjorkman, J. E., & Wolff, M. J. (2002). Regression of the mountains of mitchel polar ice after the onset of a global dust storm on mars. *Geophysical Research Letters*, *29*(21), 13-1-13-4. Retrieved from https://agupubs.onlinelibrary.wiley.com/doi/abs/10.1029/2002GL015458 doi: https://doi.org/10.1029/2002GL015458

Brown, A. J., Calvin, W. M., McGuire, P. C., & Murchie, S. L. (2010). Compact reconnaissance imaging spectrometer for mars (crism) south polar mapping: First mars year of observations. *Journal of Geophysical Research: Planets*, *115*(E2). Retrieved from https://agupubs.onlinelibrary.wiley.com/doi/abs/10.1029/2009JE003333 doi: 10.1029/2009JE003333

Brown, A. J., Piqueux, S., & Titus, T. N. (2014). Interannual observations and quantification of summertime h2o ice deposition on the martian co2 ice south polar cap. *Earth and Planetary Science Letters*, *406*, 102 - 109. Retrieved from http://www.sciencedirect.com/science/article/pii/S0012821X14005482 doi: https://doi.org/10.1016/j.epsl.2014.08.039

Calvin, W., Cantor, B., & James, P. (2017). Interannual and seasonal changes in the south seasonal polar cap of mars: Observations from my 28-31 using marci. *Icarus*, *292*, 144-153. Retrieved from https://www.sciencedirect.com/science/article/pii/S0019103516304109 doi: https://doi.org/10.1016/j.icarus.2017.01.010

Campbell, J. D., Schmitt, B., Brissaud, O., & Muller, J.-P. (2021). The detectability limit of organic molecules within mars south polar laboratory analogs. *Journal of Geophysical Research: Planets*, *126*(7), e2020JE006595. Retrieved from https://agupubs.onlinelibrary.wiley.com/doi/abs/10.1029/2020JE006595 (e2020JE006595 2020JE006595) doi: https://doi.org/10.1029/2020JE006595

Christensen, P. R., Bandfield, J. L., Hamilton, V. E., Ruff, S. W., Kieffer, H. H., Titus, T. N., ... Greenfield, M. (2001). Mars global surveyor thermal emission spectrometer experiment: Investigation description and surface science results. *Journal of Geophysical Research: Planets*, *106*(E10), 23823-23871. Retrieved from https://agupubs.onlinelibrary.wiley.com/doi/abs/10.1029/2000JE001370 doi: 10.1029/2000JE001370

Cruz Mermy, G., Schmidt, F., Thomas, I., Daerden, F., Ristic, B., Patel, M., ... Vandaele, A. (2022). Calibration of nomad on exomars trace gas orbiter: Part 3 - lno validation and instrument stability. *Planetary and Space Science*, *218*, 105399. Retrieved from https://www.sciencedirect.com/science/article/pii/S0032063321002385 doi: https://doi.org/10.1016/j.pss.2021.105399

Douté, S., & Schmitt, B. (1998). A multilayer bidirectional reflectance model for the analysis of planetary surface hyperspectral images at visible and near-infrared wavelengths. *Journal of Geophysical Research: Planets*, *103*(E13), 31367-31389. Retrieved from https://agupubs.onlinelibrary.wiley.com/doi/abs/10.1029/98JE01894 doi: 10.1029/98JE01894

Flanner, M. G., Zender, C. S., Randerson, J. T., & Rasch, P. J. (2007). Present-day climate forcing and response from black carbon in snow. *Journal of Geophysical Research: Atmospheres*, *112*(D11). Retrieved from https://agupubs.onlinelibrary.wiley.com/doi/abs/10.1029/2006JD008003 doi: 10.1029/2006JD008003

Forget, F., Hourdin, F., & Talagrand, O. (1998). Co2snowfall on mars: Simulation with a general circulation model. *Icarus*, *131*(2), 302 - 316. Retrieved from http://www.sciencedirect.com/science/article/pii/S0019103597958747 doi: https://doi.org/10.1006/icar.1997.5874

Gordon, I. E., Rothman, L. S., Hill, C., Kochanov, R. V., Tan, Y., Bernath, P. F., ... others (2017). The hitran2016 molecular spectroscopic database. *Journal*

of Quantitative Spectroscopy and Radiative Transfer, *203*, 3–69.

Grundy, W. M., & Schmitt, B. (1998). The temperature-dependent near-infrared absorption spectrum of hexagonal h2o ice. *Journal of Geophysical Research: Planets*, *103*(E11), 25809-25822. Retrieved from https://agupubs.onlinelibrary.wiley.com/doi/abs/10.1029/98JE00738 doi: 10.1029/98JE00738

Guslyakova, S., Fedorova, A., Lefèvre, F., Korablev, O., Montmessin, F., Trokhimovskiy, A., & Bertaux, J. (2016). Long-term nadir observations of the o2 dayglow by spicam ir. *Planetary and Space Science*, *122*, 1 - 12. Retrieved from http://www.sciencedirect.com/science/article/pii/S0032063315300192 doi: https://doi.org/10.1016/j.pss.2015.12.006

Hansen, G. B. (2005). Ultraviolet to near-infrared absorption spectrum of carbon dioxide ice from 0.174 to 1.8 μm. *Journal of Geophysical Research: Planets*, *110*(E11). Retrieved from https://agupubs.onlinelibrary.wiley.com/doi/abs/10.1029/2005JE002531 doi: 10.1029/2005JE002531

Hapke, B. (1981). Bidirectional reflectance spectroscopy: 1. theory. *Journal of Geophysical Research: Solid Earth*, *86*(B4), 3039-3054. Retrieved from https://agupubs.onlinelibrary.wiley.com/doi/abs/10.1029/JB086iB04p03039 doi: 10.1029/JB086iB04p03039

Herr, K. C., Forney, P. B., & Pimentel, G. C. (1972, Mar). Mariner mars 1969 infrared spectrometer. *Appl. Opt.*, *11*(3), 493–501. Retrieved from http://ao.osa.org/abstract.cfm?URI=ao-11-3-493 doi: 10.1364/AO.11.000493

Herr, K. C., & Pimentel, G. C. (1969). Infrared absorptions near three microns recorded over the polar cap of mars. *Science*, *166*(3904), 496–499. Retrieved from https://science.sciencemag.org/content/166/3904/496 doi: 10.1126/science.166.3904.496

Hourdin, F., Le Van, P., Forget, F., & Talagrand, O. (1993, 11). Meteorological Variability and the Annual Surface Pressure Cycle on Mars. *Journal of the Atmospheric Sciences*, *50*(21), 3625-3640. Retrieved from https://doi.org/10.1175/1520-0469(1993)050<3625:MVATAS>2.0.CO;2 doi: 10.1175/1520-0469(1993)050⟨3625:MVATAS⟩2.0.CO;2

Humlíček, J. (1982). Optimized computation of the voigt and complex probability functions. *Journal of Quantitative Spectroscopy and Radiative Transfer*, *27*(4), 437–444.

James, P., Thomas, P., & Malin, M. (2010). Variability of the south polar cap of mars in mars years 28 and 29. *Icarus*, *208*(1), 82-85. Retrieved from https://www.sciencedirect.com/science/article/pii/S0019103510000631 doi: https://doi.org/10.1016/j.icarus.2010.02.007

Kahre, M. A., & Haberle, R. M. (2010, June). Mars CO $_2$ cycle: Effects of airborne dust and polar cap ice emissivity. *Icarus*, *207*(2), 648-653. doi: 10.1016/j.icarus.2009.12.016

Kelly, N. J., Boynton, W. V., Kerry, K., Hamara, D., Janes, D., Reedy, R. C., ... Haberle, R. M. (2006). Seasonal polar carbon dioxide frost on mars: Co2 mass and columnar thickness distribution. *Journal of Geophysical Research: Planets*, *111*(E3). Retrieved from https://agupubs.onlinelibrary.wiley.com/doi/abs/10.1029/2006JE002678 doi: 10.1029/2006JE002678

Kieffer, H. H., Christensen, P. R., & Titus, T. N. (2006, August). CO_2 jets formed by sublimation beneath translucent slab ice in Mars' seasonal south polar ice cap. *Nature*, *442*(7104), 793-796. doi: 10.1038/nature04945

Kieffer, H. H., & Titus, T. N. (2001). Tes mapping of mars' north seasonal cap. *Icarus*, *154*(1), 162-180. Retrieved from https://www.sciencedirect.com/science/article/pii/S0019103501966709 doi: https://doi.org/10.1006/icar.2001.6670

Kieffer, H. H., Titus, T. N., Mullins, K. F., & Christensen, P. R. (2000). Mars south polar spring and summer behavior observed by tes: Seasonal cap evolu-

tion controlled by frost grain size. *Journal of Geophysical Research: Planets*, *105*(E4), 9653–9699.

Korablev, O., Bertaux, J.-L., Fedorova, A., Fonteyn, D., Stepanov, A., Kalinnikov, Y., ... others (2006). Spicam ir acousto-optic spectrometer experiment on mars express. *Journal of Geophysical Research: Planets*, *111*(E9).

Korablev, O., Fedorova, A., Villard, E., Joly, L., Kiselev, A., Belyaev, D., & Bertaux, J.-L. (2013). Characterization of the stray light in a space borne atmospheric aotf spectrometer. *Optics Express*, *21*(15), 18354–18360.

Langevin, Y., Bibring, J.-P., Montmessin, F., Forget, F., Vincendon, M., Douté, S., ... Gondet, B. (2007). Observations of the south seasonal cap of mars during recession in 2004–2006 by the omega visible/near-infrared imaging spectrometer on board mars express. *Journal of Geophysical Research: Planets*, *112*(E8).

Langevin, Y., Doute, S., Vincendon, M., Poulet, F., Bibring, J.-P., Gondet, B., ... Forget, F. (2006). No signature of clear co2 ice from the 'cryptic regions' in mars' south seasonal polar cap. *Nature*, *442*(7104), 790-792. doi: 10.1038/nature05012

Menang, K. P., Coleman, M. D., Gardiner, T. D., Ptashnik, I. V., & Shine, K. P. (2013). A high-resolution near-infrared extraterrestrial solar spectrum derived from ground-based fourier transform spectrometer measurements. *Journal of Geophysical Research: Atmospheres*, *118*(11), 5319–5331.

Millour, E., Forget, F., Spiga, A., Navarro, T., Madeleine, J.-B., Montabone, L., ... others (2015). The mars climate database (mcd version 5.2). In *European planetary science congress 2015* (Vol. 10, pp. EPSC2015–438).

Montabone, L., Forget, F., Millour, E., Wilson, R., Lewis, S., Cantor, B., ... Wolff, M. (2015). Eight-year climatology of dust optical depth on mars. *Icarus*, *251*, 65-95. Retrieved from `https://www.sciencedirect.com/science/article/pii/S0019103515000044` (Dynamic Mars) doi: https://doi.org/10.1016/j.icarus.2014.12.034

Montabone, L., Spiga, A., Kass, D. M., Kleinböhl, A., Forget, F., & Millour, E. (2020). Martian year 34 column dust climatology from mars climate sounder observations: Reconstructed maps and model simulations. *Journal of Geophysical Research: Planets*, *125*(8), e2019JE006111. Retrieved from `https://agupubs.onlinelibrary.wiley.com/doi/abs/10.1029/2019JE006111` (e2019JE006111 10.1029/2019JE006111) doi: https://doi.org/10.1029/2019JE006111

Murchie, S., Arvidson, R., Bedini, P., Beisser, K., Bibring, J.-P., Bishop, J., ... Wolff, M. (2007). Compact reconnaissance imaging spectrometer for mars (crism) on mars reconnaissance orbiter (mro). *Journal of Geophysical Research: Planets*, *112*(E5). Retrieved from `https://agupubs.onlinelibrary.wiley.com/doi/abs/10.1029/2006JE002682` doi: 10.1029/2006JE002682

Oliva, F., D'Aversa, E., Bellucci, G., Carrozzo, F. G., Ruiz Lozano, L., Altieri, F., ... Sindoni, G. (2022). Martian co2 ice observation at high spectral resolution with exomars/tgo nomad. *Journal of Geophysical Research: Planets*, *127*(5), e2021JE007083. Retrieved from `https://agupubs.onlinelibrary.wiley.com/doi/abs/10.1029/2021JE007083` (e2021JE007083 2021JE007083) doi: https://doi.org/10.1029/2021JE007083

Olsen, K., Forget, F., Madeleine, J.-B., Szantai, A., Audouard, J., Geminale, A., ... Wolff, M. (2021). Retrieval of the water ice column and physical properties of water-ice clouds in the martian atmosphere using the omega imaging spectrometer. *Icarus*, *353*, 113229. Retrieved from `https://www.sciencedirect.com/science/article/pii/S001910351830438X` (From Mars Express to Exomars) doi: https://doi.org/10.1016/j.icarus.2019.03.006

Piqueux, S., Kleinböhl, A., Hayne, P. O., Kass, D. M., Schofield, J. T., & McCleese, D. J. (2015). Variability of the martian seasonal co2 cap extent

over eight mars years. *Icarus*, *251*, 164-180. Retrieved from https://www.sciencedirect.com/science/article/pii/S0019103514006022 (Dynamic Mars) doi: https://doi.org/10.1016/j.icarus.2014.10.045

Quirico, E., & Schmitt, B. (1997). Near-infrared spectroscopy of simple hydrocarbons and carbon oxides diluted in solid n2and as pure ices: Implications for triton and pluto. *Icarus*, *127*(2), 354 - 378. Retrieved from http://www.sciencedirect.com/science/article/pii/S0019103596956638 doi: https://doi.org/10.1006/icar.1996.5663

Schmidt, F., Douté, S., Schmitt, B., Vincendon, M., Bibring, J.-P., & Langevin, Y. (2009). Albedo control of seasonal south polar cap recession on mars. *Icarus*, *200*(2), 374 - 394. Retrieved from http://www.sciencedirect.com/science/article/pii/S0019103508004351 doi: https://doi.org/10.1016/j.icarus.2008.12.014

Shkuratov, Y., Starukhina, L., Hoffmann, H., & Arnold, G. (1999). A model of spectral albedo of particulate surfaces: Implications for optical properties of the moon. *Icarus*, *137*(2), 235-246. Retrieved from https://www.sciencedirect.com/science/article/pii/S0019103598960353 doi: https://doi.org/10.1006/icar.1998.6035

Singh, D., & Flanner, M. G. (2016). An improved carbon dioxide snow spectral albedo model: Application to martian conditions. *Journal of Geophysical Research: Planets*, *121*(10), 2037-2054. Retrieved from https://agupubs.onlinelibrary.wiley.com/doi/abs/10.1002/2016JE005040 doi: 10.1002/2016JE005040

Szantai, A., Audouard, J., Forget, F., Olsen, K. S., Gondet, B., Millour, E., ... Bibring, J.-P. (2021). Martian cloud climatology and life cycle extracted from mars express omega spectral images. *Icarus*, *353*, 114101. Retrieved from https://www.sciencedirect.com/science/article/pii/S0019103520304462 (From Mars Express to Exomars) doi: https://doi.org/10.1016/j.icarus.2020.114101

Trokhimovskiy, A., Fedorova, A., Korablev, O., Montmessin, F., Bertaux, J.-L., Rodin, A., & Smith, M. D. (2015). Mars' water vapor mapping by the spicam ir spectrometer: Five martian years of observations. *Icarus*, *251*, 50–64.